Modeling and Experimental Validation of CFRP-Metal Joints Utilizing 3D Additively Manufactured Anchors

ASME Journal of Manufacturing Science and Engineering
Online journal at:
https://asmedigitalcollection.asme.org/manufacturingscience

Modeling and Experimental Validation of CFRP–Metal Joints Utilizing 3D Additively Manufactured Anchors

Giorgio De Pasquale[1]
Smart Structures and Systems Lab,
Department of Mechanical and Aerospace Engineering,
Politecnico di Torino,
Corso Duca degli Abruzzi 24,
10129 Torino, Italy
e-mail: giorgio.depasquale@polito.it

Antonio Coluccia
Smart Structures and Systems Lab,
Department of Mechanical and Aerospace Engineering,
Politecnico di Torino,
Corso Duca degli Abruzzi 24,
10129 Torino, Italy
e-mail: antonio.coluccia@polito.it

The joining techniques between carbon fiber reinforced polymer (CFRP) and metal are of great importance in many areas of structural mechanics where the optimization of weight, rigidity, and strength is a necessity (such as aeronautics, vehicles, energy generation, and biomechanics). As a result, several types of metal–composite joints have been manufactured using different methods, with the 3D metal anchor solution attracting significant attention. This study evaluates different anchor geometries applied to single lap joints through preliminary finite element method (FEM) simulations and experimental validation on joints between CFRP and Inconel 625 produced via a laser beam powder bed fusion (LB-PBF) additive process. The models proposed increase in complexity. The homogenization process is employed to determine the equivalent properties of the joint region that is occupied by metal anchors and CFRP. The model also supports topology parametrization to assess the impact of anchor geometry on structural properties. The study provides experimental validation of joint strength under tensile load for various anchoring surface topologies. [DOI: 10.1115/1.4063110]

Keywords: additive manufacturing, advanced materials and processing, assembly, design for manufacturing, laser processes, modeling and simulation

1 Introduction

Over the past few decades, composite structures have become widespread across many industries. Consequently, the need to join metallic components with composites has become a significant concern for designers. In Ref. [1], a comprehensive collection of the most critical jointing techniques is provided. Adhesive bonding can be used for composite–metal joints, but it is more commonly utilized for composite–composite joints, producing either co-bonded (cured laminate with wet laminate) or co-cured (wet laminate with wet laminate) joints [2]. In the case of thin composite panels, some solutions have been proposed that involve embedding thin metallic inserts into the laminate, providing efficient load transfer to the fibers [3]. The ultrasonic additive manufacturing (AM) process for creating an interlocking joining system between carbon fiber reinforced polymer (CFRP) and metal has been explored in Ref. [4]. Innovation based on unconventional methods can also be found in Ref. [5], where ultrasonic spot welding is utilized to join CFRP and aluminum alloy. Riveting and bolting are widely used in the aerospace industry, where titanium rivets are often employed to join the two different materials. This approach enables material recycling after service and achieves high mechanical properties. However, fatigue-related failure issues can occur, particularly in regards to fiber damage. Hybrid strategies that utilize metal protrusions and rivets or bolts have also been explored in the literature [6,7]. The so-called "through-the-thickness reinforcement" strategies for composite–composite and composite–metal joints have been reviewed in Ref. [8], where different techniques for the application and insertion of metallic pins are presented. Furthermore [9], showcases interesting designs and techniques related to z-pins exclusively. In the lightweight aviation industry, a novel hybrid joining technique for CFRP has been presented in Ref. [10]. The technique involves welding metallic pins onto the metallic surface and embedding dry carbon fibers in the resulting space. The joints are then subjected to resin infiltration and curing processes, followed by tensile load testing. A similar approach can be seen in Ref. [11], where CFRP–CFRP parts are joined using z-pins made of steel and titanium, which are placed on a plate using the cold metal transfer welding process. These joints are then tested for fatigue failure. The concept is further explored in Ref. [12], where the influence of different pin geometries is investigated in a CFRP-titanium joint. There have been numerous investigations from Refs. [13–20] focused on pinned joints, examining their mechanical properties such as strength, damage tolerance, and failure mechanisms, as well as the effects of fibers undulation or pin topologies. z-pins are not limited to single or double lap joints, as seen in Ref. [21], where they are also used for hat joints. There is also a significant interest in modeling and optimizing metal pins, as seen in Refs. [22,23], where the effects of geometry, load, and supports on their mechanical properties and fatigue failure modes are explored. As previously stated, riveting is utilized as an alternative to pinning. In Ref. [24], the mechanical performance of a single rivet joint is studied, and the effects of combining riveting and pinning on fatigue performance

[1]Corresponding author.

Manuscript received May 16, 2023; final manuscript received July 25, 2023; published online August 29, 2023. Assoc. Editor: Martine Dubé.

are discussed in Ref. [7]. A completely different configuration can be found in Ref. [25], where no form of reinforcement or pin is used. In this technique, resin hardens within drilled holes in the metal specimen, allowing it to be attached to a CFRP end through a double lap joint. Various studies have investigated CFRP–CFRP bonding techniques based on metal plates with spikes that penetrate the composite plates [26–30]. The focus of these studies includes fatigue behavior, damage processes, failure modes, and other experimental targets. Additionally, CFRP–metal joints can also be designed using anchoring elements other than pins. In Ref. [31], the authors present a design for a Ti6Al4V–CFRP double lap joint based on electron beam surface processes to create the anchors. A similar design is presented in Ref. [32], where AM methods are used to construct aluminum anchors. In Ref. [33], the authors provide geometrical optimization of the anchors in terms of height and angular orientation. Another notable design is proposed in Ref. [34]: steel lattice structures are generated on a steel plate using selective laser melting, and then stacks of fibers with different orientations are pressed onto the lattice and infiltrated. The accuracy of the building process and mechanical strength are analyzed. The design in Ref. [35] is based on interlocking structures constructed through AM, linked to a composite end through resin hardening in the voids created by the metallic part. The design process focuses on failure mechanisms. The manufacturing of such joints, based on interlocking anchors or protrusions, is greatly benefited by AM, as can be seen from the aforementioned papers. Their concept design can also be related to lattices, as they are repetitive structures with a predefined relative density [36–43].

The authors have already conducted research on the CFRP–metal joint with the objective of optimizing the 3D anchoring strategy. In Refs. [44–46], the shape of this joint has been described using two finite element modeling (FEM) approaches. The first model defines the anchor's geometry accurately, while the second model employs a mixing rule to calculate equivalent properties of a medium material in the region where the two materials intersect and the metal anchors penetrate the CFRP. This paper presents a more precise and trustworthy joint model, backed by experimental validation. By applying the homogenization process to the representative volume element (RVE), equivalent material properties are calculated to predict the joint's overall behavior. The RVE consists of a single metal anchor and the surrounding CFRP volume. The simulation results are compared, for different anchor geometries, to the predictions of the simplified models and experimental measurements. The joints are manufactured by laminating the CFRP and co-curing metal inserts, which were previously fabricated with In625 through the laser-based powder bed fusion process. The joint's overall mechanical properties are determined by comparing results and discussing observed failure modes.

2 Joint Samples and Numerical Modeling

The CFRP–metal joint was designed based on the sample configuration specified in the ISO 22841 standard [47], which is used for conducting tensile tests to evaluate the tensile lap-shear joint.

2.1 Joint Samples Design. The single lap joint sample has dimensions of $110 \times 20 \times 6$ mm^3, while the two original metal and CFRP parts have dimensions of $70 \times 20 \times 3$ mm^3. The joint area measures 30×20 mm^2. The overall sample dimensions are illustrated in Fig. 1.

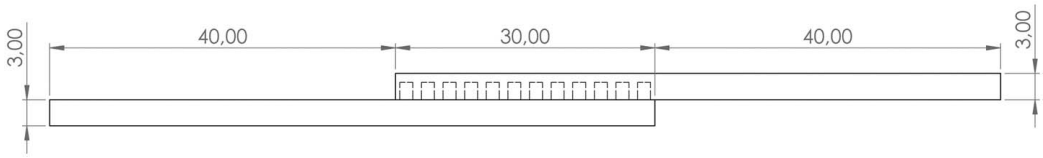

Fig. 1 Overall dimensions (in millimeters) of the joint sample (with block anchors configuration); the uniform width is 20 mm, materials are Inconel 625 and CFRP

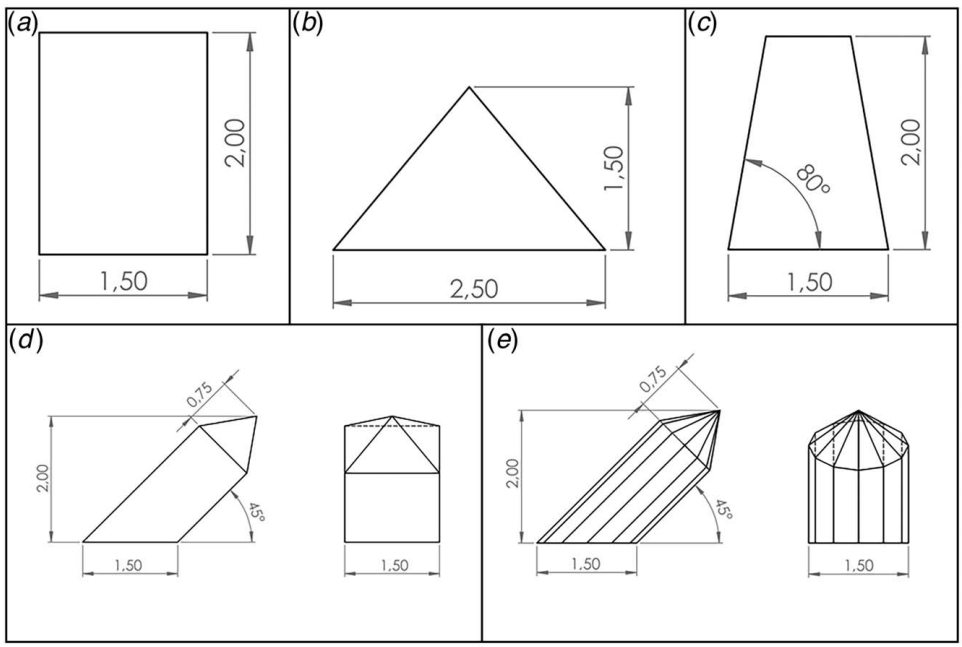

Fig. 2 Anchors geometries and dimensions (in millimeters): (*a*) block, (*b*) pyramid, (*c*) pyramid trunk, (*d*) up/down-oriented spiked block, and (*e*) up/down-oriented spiked elliptical cylinder

Seven different anchor geometries were analyzed, including block, pyramid, pyramid trunk, up/down-oriented spiked block, and up/down-oriented spiked elliptical cylinder (modeled with a certain number of prismatic faces). The anchors shaped with spiked block and spiked elliptical cylinder are oriented at ±45 deg (up/down) relative to the plane of load direction. The dimensions of all the anchors are shown in Fig. 2. In all joint configurations, 12×8 anchors are placed with uniform distribution along the overlapped area. The initial three anchor geometries, namely, blocks, pyramids, and trunks, are selected to examine how the shape of the anchors can influence the performance of the joints and their failure mode. The remaining four anchor geometries, including up/down-oriented spiked blocks and elliptical cylinders, are of interest for investigating how the orientation of the anchor relative to the load direction affects the obtained results.

Table 1 Material properties used for Inconel 625 and CFRP in the simulations

Inconel 625		CFRP	
E (MPa)	180,000	$E_x = E_y$ (MPa)	35,000
		E_z (MPa)	3000
G (MPa)	69,230	$G_{yz} = G_{xz}$ (MPa)	1154
		G_{xy} (MPa)	1154
ν	0.3	$\nu_{xy} = \nu_{yz} = \nu_{xz}$	0.3

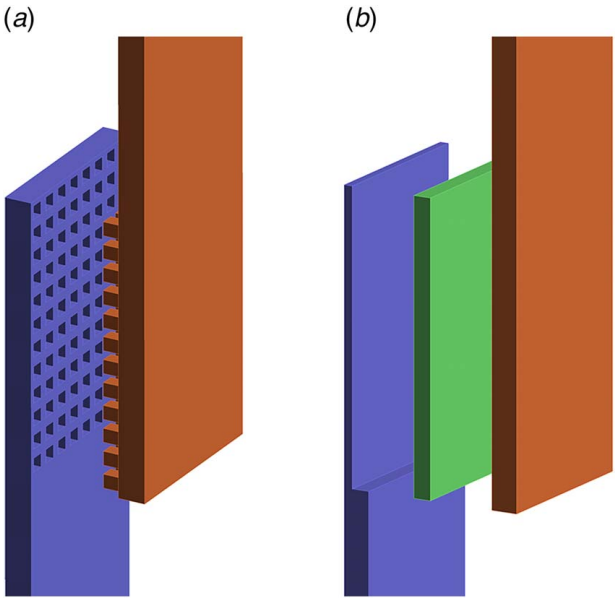

Fig. 3 Previous models geometrical configurations: (*a*) 2 volumes model and (*b*) 3 volumes mixed model; in both pictures, left part is made of In625, right part is made of CFRP, and intermediate part is the medium material

2.2 Numerical Modeling. The static structural behavior of the joint is simulated using three different models, each with a varying level of complexity. The authors, in Ref. [44], have introduced two models: the "2-volumes model" and the "3-volumes mixed model." The "3-volumes homogenized model" is described in this section. All the models are valid in the elastic regime, which is limited to the initial part of the force–displacement curve of the joint. Based on further experimental tests, the linear region of the samples examined is identified before the transition to the nonlinearity.

The "2-volumes model" replicates the nominal geometry of the two materials being joined, including the 3D anchors. Two volumes are utilized to simulate the two materials (In625 and CFRP), as shown in Fig. 3(*a*). The "3-volumes mixed model" utilizes the mixture rule to define a third material, which represents the mechanical properties of the intermediate region where the anchors are embedded into the CFRP (Fig. 3(*b*)). This model does not replicate the actual shape of the anchors, resulting in a simplified joint geometry and fewer degrees-of-freedom, thus reducing computational time.

The "3-volumes homogenized model" is based on the homogenization process, which is commonly used in the numerical analysis of micromechanics of composites and lattice structures [48,49]. The model is defined by identifying the RVE, which, in this case, is associated with the single metal anchor and the surrounding composite. The metal part is defined with isotropic properties, while the

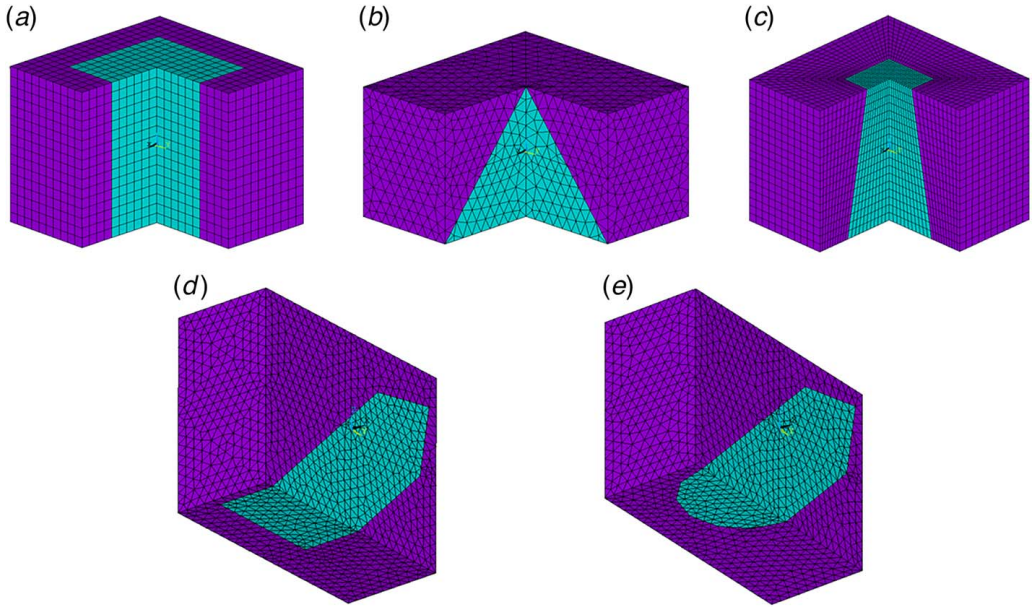

Fig. 4 Finite element discretization of the RVEs for the different anchor geometries (section view): (*a*) block, (*b*) pyramid, (*c*) trunk, (*d*) up/down-oriented spiked block, and (*e*) up/down-oriented spiked elliptical cylinder. External volume is for Inconel 625 and internal volume is for CFRP.

Fig. 5 Joint model configuration: lower elements represent the In625, the upper ones represent the CFRP, and intemediate elements represent the homogenized material (the height varies according to the RVE size along *z*-direction)

composite material is defined with the orthotropic properties of the fiber–matrix composition.

Periodic boundary conditions are applied to the RVE to determine the averaged loadings that are used to evaluate the equivalent stiffness matrix. Finally, the equivalent mechanical properties in terms of elastic and shear moduli and Poisson's ratios are extracted for the orthotropic medium. ANSYS APDL macros are used for selecting and grouping the RVE nodes, applying boundary conditions, and analyzing the results to obtain equivalent properties.

This process is applied to every anchor geometry, with the homogenization process applied only once to the up- and down-oriented blocks and cylinders, as the model is insensitive to anchor orientation. The main advantage of this model over the "3-volumes mixed model" based on material properties weighting is that anchor shape and type also contribute to defining the equivalent material, in addition to the anchor volume. On the other hand, the homogenized model requires far less computational effort than the "2-volumes model" for joint simulation.

The meshing associated with the RVE used in the homogenization process is shown in Fig. 4. Regular SOLID 186 hexahedral elements are used for simpler block and trunk geometries, whereas SOLID 187 tetrahedral elements are used for pyramid and up/down-oriented blocks. The element size ranges between 0.12 and 0.15 mm, and element distortion is controlled, particularly for up/down-oriented anchors, which require dividing the RVE into eight parts. The isotropic properties of In625 and the orthotropic properties of CFRP are listed in Table 1. The same properties are used for both the homogenization process on the RVE and the overall joint simulation with the equivalent medium material.

The equivalent properties of the medium material that represents the joining region are obtained and reported in Sec. 4. Then, the simulation of the tensile loading of the entire joint is conducted using SOLID 186 hexahedral elements with an average dimension of 1.5 mm. The metal end of the joint is fully constrained, while the CFRP end is loaded with a force of 125 N along the axial direction. To prevent bending loads on the sample, the translational degrees-of-freedom in the width and depth directions at the loaded end of the joint are blocked. However, bending effects typical of single lap joints are taken into account in the joining section for high deformations. The model constraints are defined to accurately replicate the experimental setup, as described in the next section. The configuration of the model is illustrated in Fig. 5. The axial elongation of the sample along the load direction is calculated, as well as the linear force–displacement curve representing the joint behavior. The same calculation is performed with the two simplified models described earlier. Comparing the simulation results with the experimental results reported in the next sections enables an assessment of the accuracy of the three models.

Table 2 Process parameters applied to the RenAM 500M system for the fabrication of the In625 joint parts

Layer	Hatch	Border
Layer thickness: 40 μm	Power: 190 W Hatch distance: 110 μm Point distance: 90 μm Exposure time: 100 μs Hatch offset: −20 μm	Numbers of border: 1 Power: 190 W Point distance: 90 μm Exposure time: 100 μs

3 Experimental Validation

3.1 Sample Fabrication. The sample manufacturing process composes of two stages. First, the metal part is produced using the laser beam powder bed fusion process. Second, the metal part is manually integrated into the CFRP during the forming process, using the interlocking technique of the carbon fibers with the metal anchors. The CFRP component of the joint is manufactured by utilizing a manual process of applying epoxy resin to a dry twill carbon fiber weave.

The Renishaw AM 500M machine with Inconel 625 is utilized to fabricate the metal parts. With the exception of the block and trunk geometries, all anchors are self-supporting during the part growth, and hence do not require supporting structures. The process parameters are listed in Table 2, and the as-built configuration of the samples is shown in Figs. 6 and 7. Subsequently, the samples are mechanically released from the platform by wire cutting, and temporary supports are removed by sandblasting. All sample surfaces are subjected to sandblasting to improve finishing. In total, six samples have been produced per geometry.

The second phase of the joint manufacturing process involves the creation of the CFRP side. The forming process entails the simultaneous co-curing of CFRP with the metal joining volume. Twill carbon fiber is utilized in conjunction with bi-component epoxy resin. The lamination process necessitates the initial fabrication of a flat mold (Fig. 8(*a*)) that allows for the proper stacking of plies and guides the resin flow to the required areas. Polyvinyl alcohol release agent is applied to exposed surfaces to facilitate the removal of the sample from the mold. The first forming operation involves the positioning of the carbon fibers among the anchors with mutual engagement (Fig. 8(*b*)). Then, twill fiber sheets are

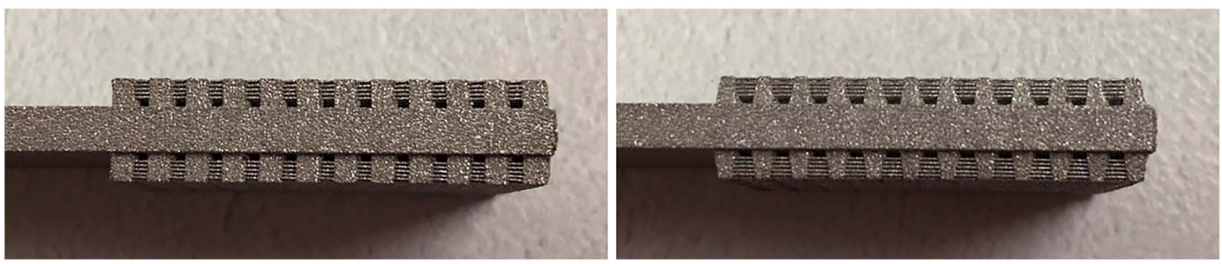

Fig. 6 As-built block (right) and trunk (left) anchors applied to joint sample surfaces with their temporary supporting structures

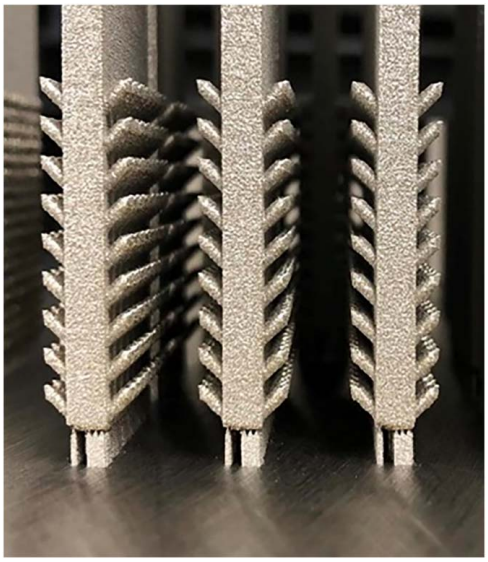

Fig. 7 As-build samples with down-oriented spiked cylinder anchors. No supports are provided in this case since anchors orientation is sufficient to guarantee self-supporting. The same condition occurs for pyramids and other oriented spiked anchors.

piled and impregnated with epoxy resin until a 3 mm-thick CFRP laminate is achieved (i.e., the same thickness as the metal part of the joint). The resin polymerization process takes 24 h at ambient temperature and pressure. The final joint is shown in Fig. 8(*c*). When the CFRP curing process is completed, the sample contours are refined using a band saw to attain the nominal dimensions. Figure 9 depicts a sample for each anchor geometry, and the sample numbers are listed in Table 3.

3.2 Experimental Setup. Experimental tests were conducted to evaluate the force–displacement static response of the joint and to correlate this property to the specific 3D anchor type. Additionally, the force–displacement curves were utilized to validate model predictions. Finally, the joint damage observed during the tests was used to investigate the failure mode associated with the anchor types.

Tensile tests were performed on manufactured samples using a servohydraulic machine, specifically the Instron 8801, with a maximum load capacity of 100 kN. The joint underwent shear loading when subject to a tensile load. To prevent sample bending caused by the misalignment between the two anchoring points, a spacer was used to restore nominal alignment. The tests were performed in displacement control mode at a velocity of 1 mm/min, while the tensile force was recorded. Figure 8(*d*) depicts the test setup.

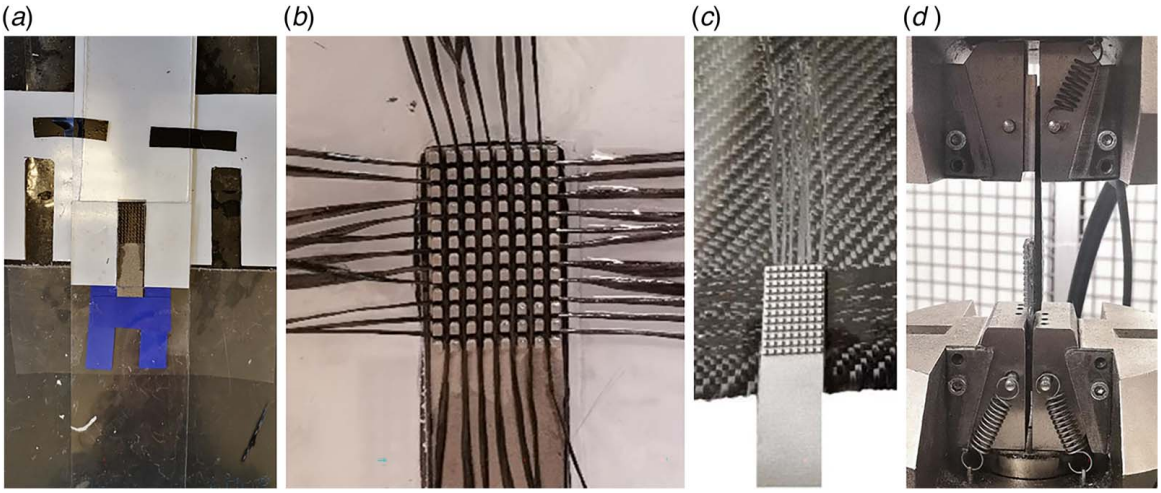

Fig. 8 Metal–CFRP joint fabrication process: (*a*) the In625 part is inserted into the mold for lamination, (*b*) the carbon fibers are engaged among the metal anchors, (*c*) the joint sample is released after the resin curing, and (*d*) the sample is installed on the tensile testing machine

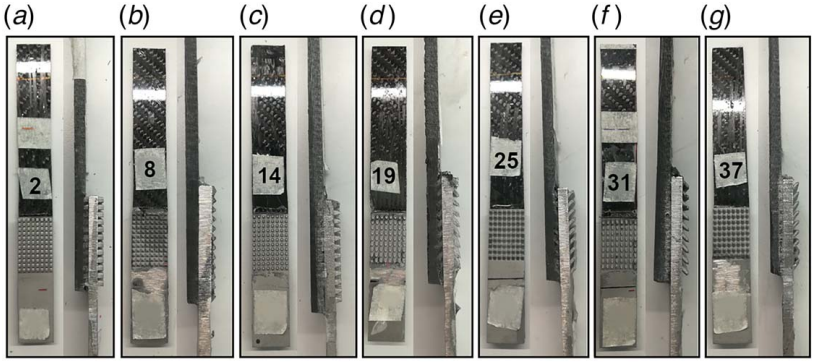

Fig. 9 Metal–CFRP samples at the end of the fabrication process: (*a*) block, (*b*) pyramid, (*c*) pyramid trunk, (*d*) down-oriented spiked block, (*e*) up-oriented spiked block, (*f*) down-oriented spiked elliptical cylinder, and (*g*) up-oriented spiked elliptical cylinder

Table 3 Samples numbering with reference to the anchors geometry

Anchor geometry	Block	Pyramid	Trunk	Down-oriented spiked block	Up-oriented spiked block	Down-oriented spiked elliptical cylinder	Up-oriented spiked elliptical cylinder
Sample number	1–6	7–12	13–18	19–24	25–30	31–36	37–42

4 Results and Discussions

The static force–displacement curves associated with different metal anchors are illustrated in Fig. 10. The stiffness values calculated from the different models are presented in Table 4. The experimental stiffness was averaged among the curves interpolated with the least-square method applied to the experimental data. The linear region of validity of the FEM models is limited to 0.3 mm for

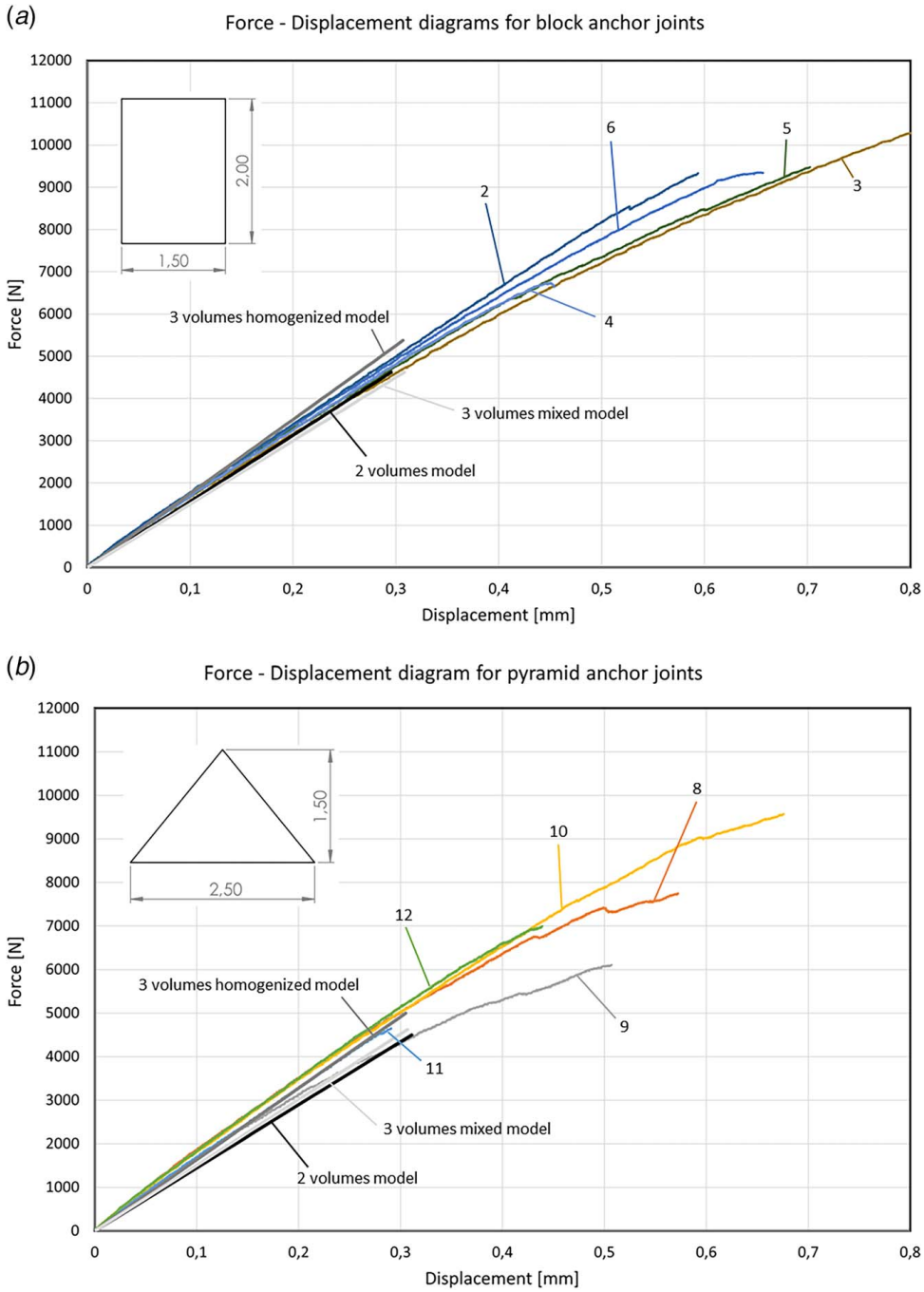

Fig. 10 Force–displacement diagrams from experimental tests and simulations for different anchor joint types: (*a*) block, (*b*) pyramid, (c) trunk, (*d*) down-oriented spiked block, (*e*) up-oriented spiked block, (*f*) down-oriented spiked elliptical cylinder, and (*g*) up-oriented spiked elliptical cylinder

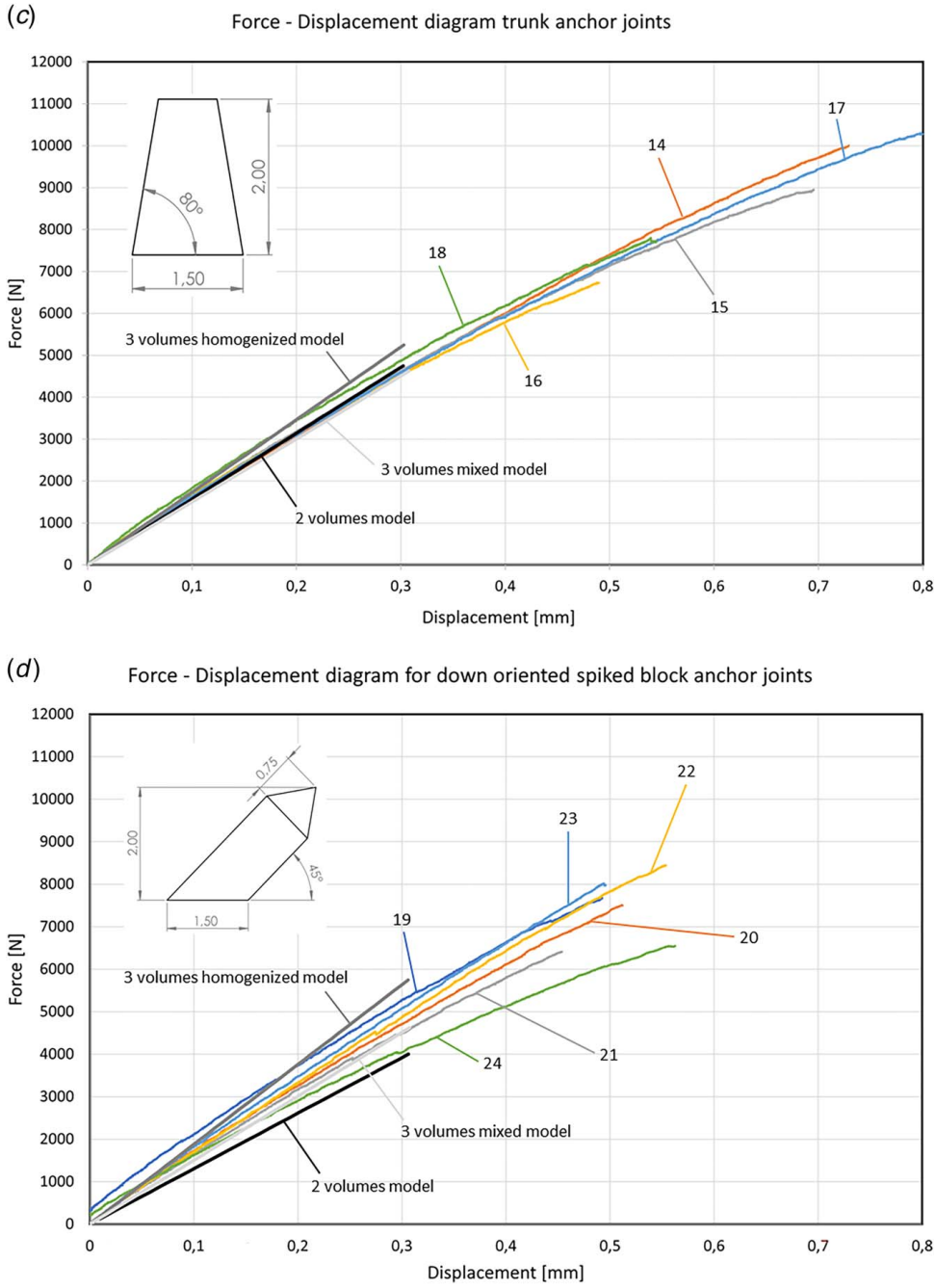

Fig. 10 ***Continued***

all the samples, based on the experimental results. The percentage errors of the measured and calculated forces were estimated into the range of linear displacement for every model as

$$E(\%) = \frac{F_{\mathrm{FEM}} - F_{\mathrm{EXP}}}{F_{\mathrm{EXP}}} \times 100$$

The diagrams in Fig. 11 display the error estimation averaged over ten measurements for every model and anchor geometry.

The proposed models are capable of predicting the behavior of joints with varying levels of accuracy; furthermore, each model presents its own advantages and disadvantages. As a general consideration, the 2-volumes model, with the exception of oriented block anchors, is always the stiffer option. On the other hand, the 3-volumes mixed model is always the least stiff, except for the oriented block anchor, where the 2-volumes model is the least stiff. The 3-volumes homogenized model tends to fall within the spectrum defined by the other two, although the medium material properties can be modulated with high accuracy by means of simulation parameters.

The comparison of stiffness values reported in Table 4 shows that, for the first three anchor geometries considered (block, pyramid, and trunk), both the 2-volumes and 3-volumes mixed models provide the best agreement with experimental data (expressed through the least-square method). The 3-volumes homogenized model provides the optimal fit for both pyramid and trunk anchors, as well as a satisfactory fit for block. However, the trends for oriented anchors are distinct. It is worth noting that the outcomes obtained from oriented blocks and cylinders are comparable for the 3-volumes homogenized model, which indicates the consistency of the model. The same conclusion can also be made for the 3-volumes mixed model. These models consider the existence of a

(*e*) Force - Displacement diagram for up oriented spiked block

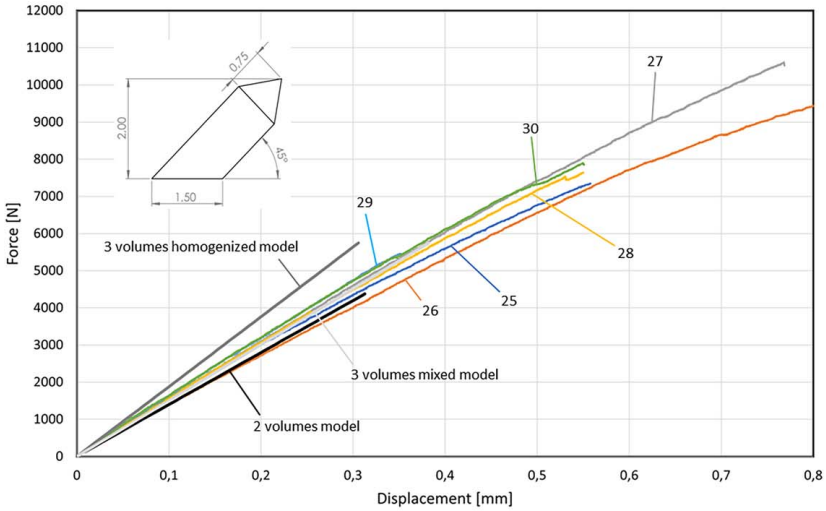

(*f*) Force - Displacement diagram for down oriented spiked elliptical cylinder acnchor joints

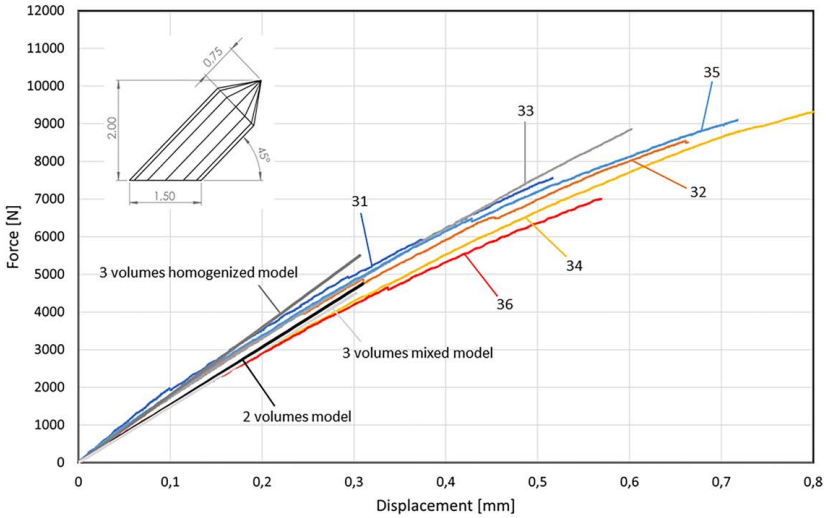

(*g*) Force - Displacement diagram for up oriented spiked elliptical cylinder anchor joints

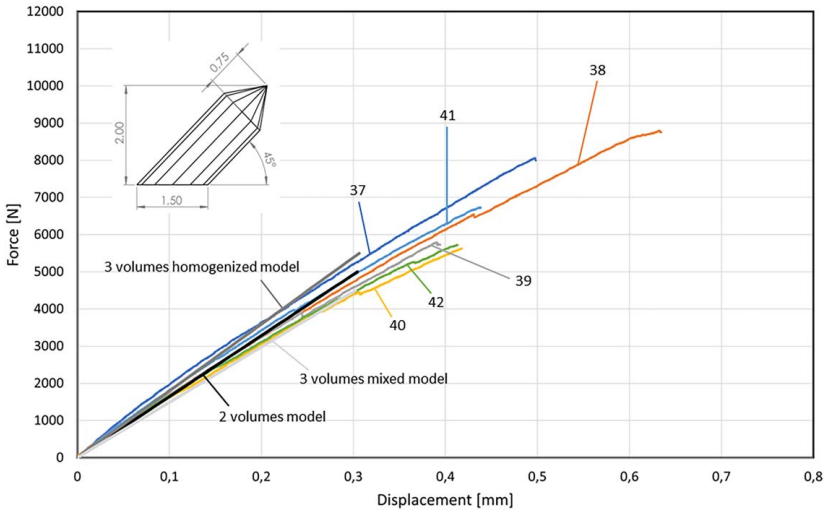

Fig. 10 ***Continued***

Table 4 Stiffness values calculated with the three numerical models and from experimental results by means of the least-square method for every anchor geometry and percent error with experimental results

	k (N/mm)				Percent error (%)		
Anchor geometry	2-volumes model	3-volumes mixed model	3-volumes homogenized model	Experimental (least-square)	2-volumes model	3-volumes mixed model	3-volumes homogenized model
Block	15,654.35	15,006.00	17,512.89	16,803.27	−2.82	−6.84	8.72
Pyramid	14,473.87	15,073.86	16,384.85	16,872.46	−7.08	−3.23	5.18
Trunk	15,713.39	15,021.33	17,329.58	15,868.58	−4.01	−8.24	5.86
Down-oriented spiked block	13,061.65	15,041.21	18,791.06	16,819.16	−16.90	−4.31	19.55
Up-oriented spiked block	13,988.65			15,730.29	−6.86	0.15	25.12
Down-oriented spiked elliptical cylinder	15,339.78	14,833.61	17,953.32	15,470.19	−2.27	−5.49	14.38
Up-oriented spiked elliptical cylinder	16,428.45			16,825.60	3.55	−6.50	13.16

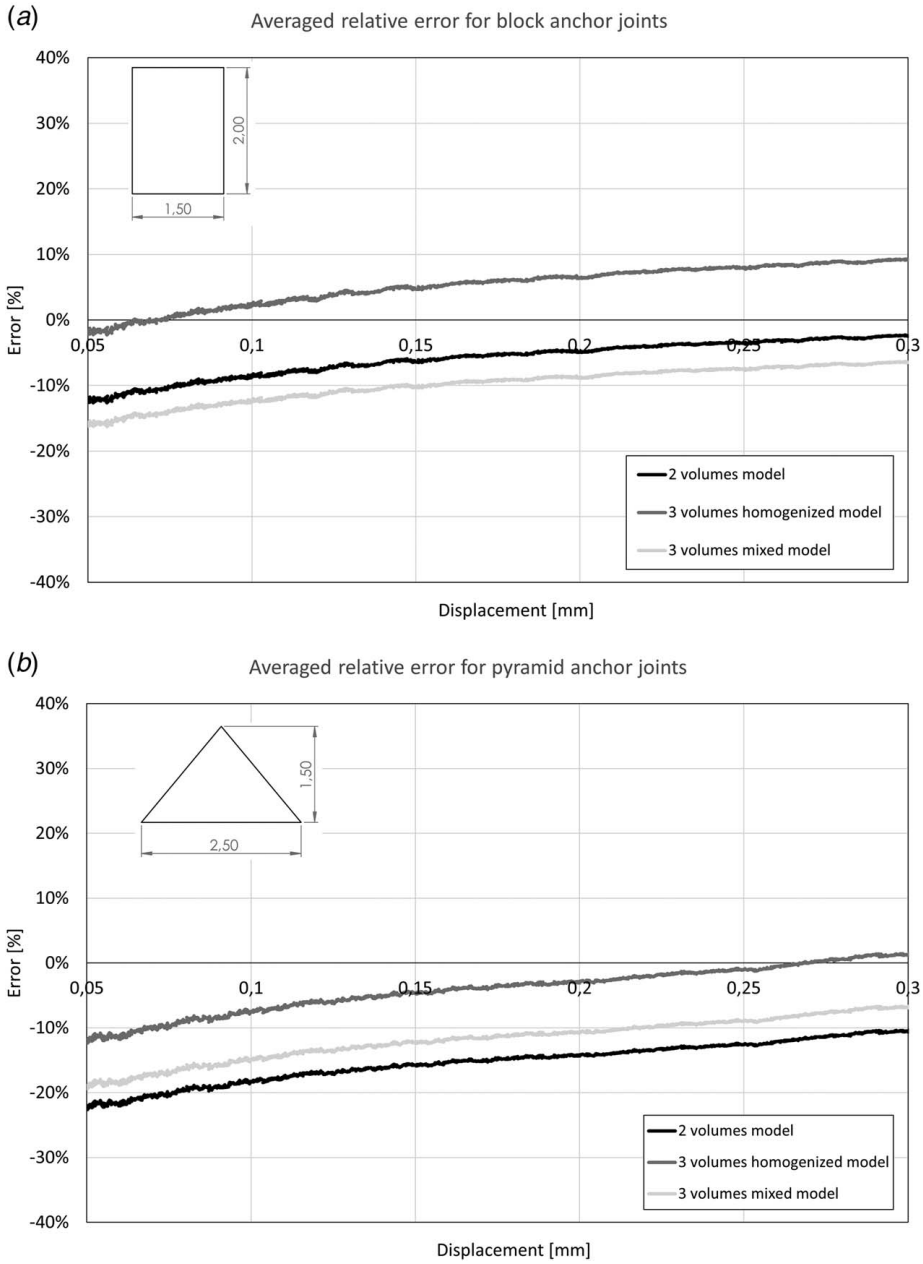

Fig. 11 Percent error of instant force between experiments and "2-volumes model" (black), "3-volumes mixed model" (light gray), and "3-volumes homogenized model" (dark gray) for samples with different anchor joint types: (*a*) block, (*b*) pyramid, (*c*) trunk, (*d*) down-oriented spiked block, (*e*) up-oriented spiked block, (*f*) down-oriented spiked elliptical cylinder, and (*g*) up-oriented spiked elliptical cylinder

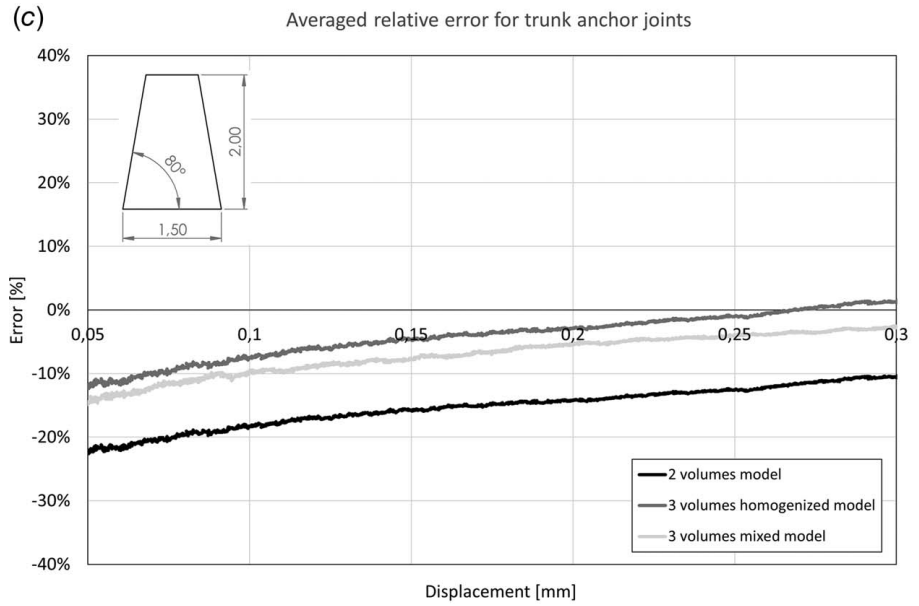

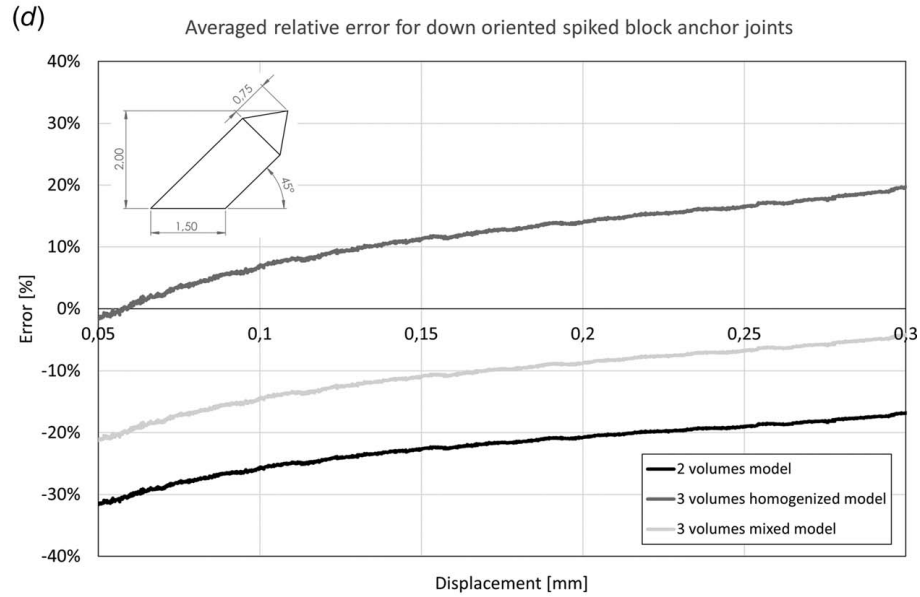

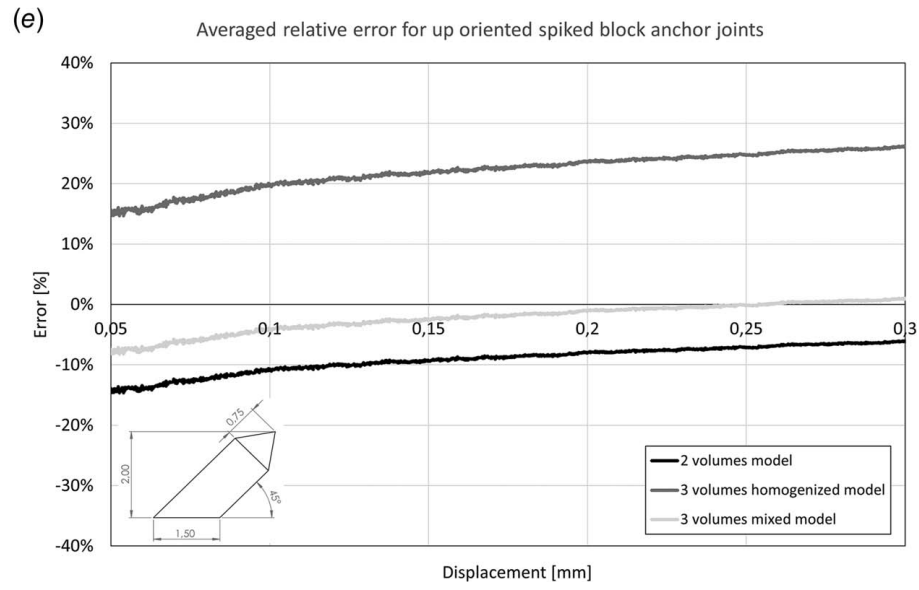

Fig. 11 ***Continued***

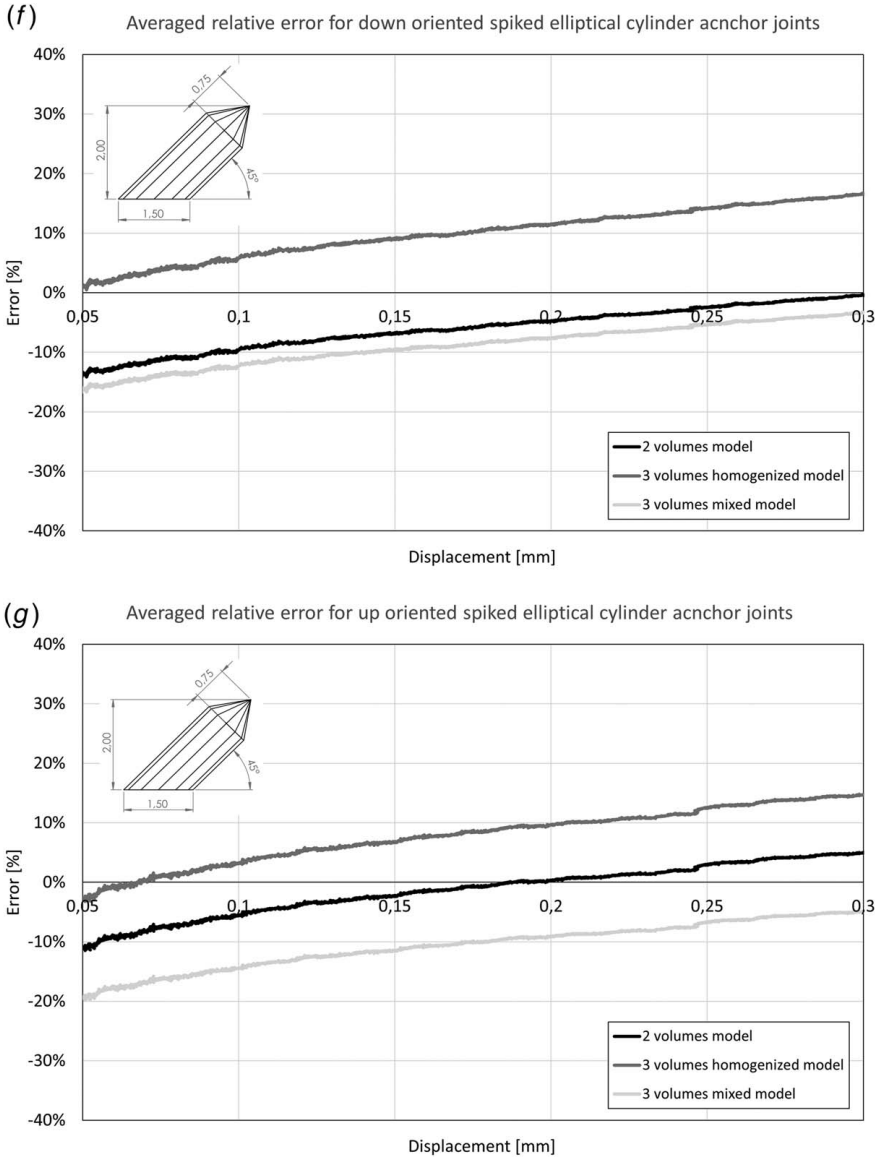

Fig. 11 ***Continued***

second phase (metal) within a primary phase (CFRP), and the equivalent material properties are determined based on this assumption. Nonetheless, the limitation of these models is that the orientation of the anchors cannot be taken into account. The only feasible enhancement that can be made is to use homogenization rather than the mixture rule, which involves the consideration of the RVE stiffness instead of volume when determining the medium properties.

The stiffness results obtained from the 2-volumes model exhibit high variability, especially for the oriented block anchors. This variability can be attributed to the need to build an accurate 3D model of the joint, which introduces mesh irregularities and element distortion. These issues are more pronounced in the 2-volumes model and are further exacerbated by the intricate geometry of the anchors, with oriented anchors being particularly problematic. Another factor contributing to the error in stiffness results is the nonlinearity of experimental curves even in the range considered (0–0.3 mm). The least-squares fitting used to determine the slopes takes into account the weak non-linear effects of the samples tested, which are visible in the force–displacement diagrams presented in Fig. 10. Therefore, force–displacement diagrams obtained from experimental data are not linear, resulting in lower experimental averaged fit slopes.

Henceforth, the comparison between the force errors simulated and measured, as shown in Fig. 11, provides additional information. In the linear displacement range of 0–0.3 mm, the 2-volumes model yields an error range of −7.0% to +3.5% (except down-oriented spike blocks anchors), the 3-volumes mixed model from −6.8% to +8.2%, and the 3-volumes homogenized model from +5.1% to +25.1%.

The results of the experimental tests are presented in Fig. 12, showing the maximum load achieved during the tests, which corresponds to the failure initiation or joint sample failure. Among the different types of joints tested, block anchors exhibit the highest ultimate load (9327.32 N), despite not having the highest experimental stiffness (see Table 4). The behavior of trunk anchor joints is quite similar to that of block anchors, with minor differences in terms of the maximum load and stiffness obtained. The failure modes for these joints are identical: the fibers break at the CFRP–metal interface, leaving the anchors intact. Some instances of local delamination (cohesive failure) between plies are observed in the joint area. Adhesive and cohesive failure modes of the joints are shown in Figs. 13(*a*) and 13(*b*), respectively.

Pyramid anchor joints exhibit the lowest maximum load (6794.36 N), but at the same time, the highest experimental

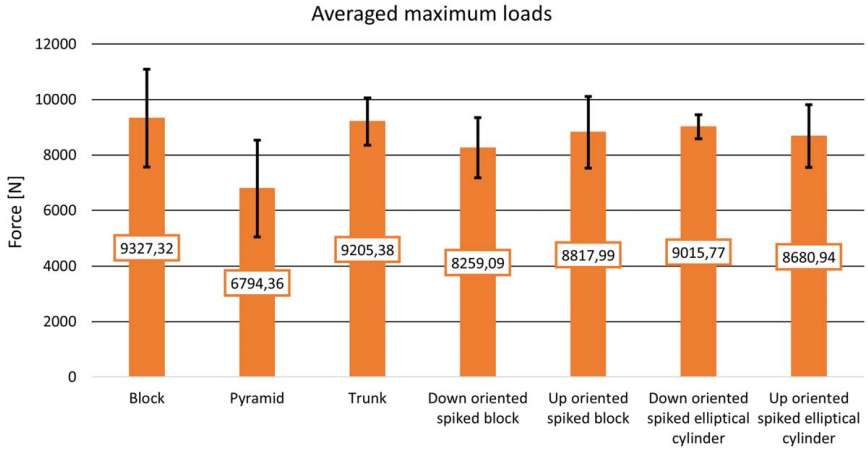

Fig. 12 Maximum load averaged among samples that is achieved with each anchor geometry

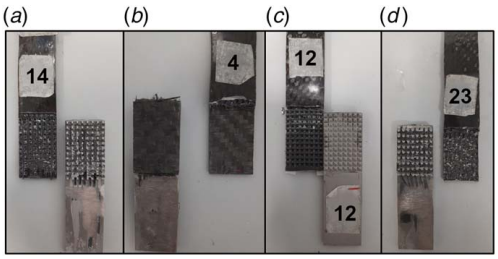

Fig. 13 Examples of adhesive and cohesive failure modes of the joints (sample number reported). (*a*) CFRP–metal interface adhesive failure with block and trunk anchors joint, (*b*) cohesive delamination failure with block and trunk anchor joints, (*c*) adhesive failure with complete detachment of the CFRP with pyramid anchors joint, and (*d*) partial adhesive failure with oriented anchors joint with exposed carbon fibers.

averaged stiffness due to their failure mode, which consists of complete adhesive detachment of the CFRP from the metal surface (Fig. 13(*c*)). By adjusting the parameters defining the pyramid's geometry, such as increasing the height of the anchors and providing more space to accommodate the fibers between the anchors, better results can be achieved. The failure mode associated with pyramid anchors is not related to progressive interface deterioration and happens abruptly.

There are no significant differences between up/down-oriented anchors, especially in terms of maximum load (ranging from 8000 to 9000 N). Their failure mode is quite similar to that of block and trunk joints, i.e., partial adhesive failure (as shown in Fig. 13(*d*)), without any exceptions among the samples. The fibers present in the space between the anchors tend to remain adhered to the metal, while the CFRP fails under the applied load.

5 Conclusion

This paper presents simulation methods and models for predicting the force–displacement characteristics of metal–CFRP joints based on 3D anchors. The proposed models vary in complexity, resulting in different levels of accuracy and detail. The comparison of experimental results on joint samples with different anchor geometries allows us to validate the model predictions and evaluate the performance of each interface geometry. Our results show that block and trunk anchors provide the best performance, with similar ultimate strength and structural stiffness. Cohesive failure or partial adhesive failure with carbon fibers exposure demonstrates the effective engagement of the carbon fibers with the metal surface. The orientation of the anchors aligned or against the load direction does not significantly affect the final performance of the joint. The pyramid anchor shape exhibits the lowest strength and complete adhesive failure of the joint, preventing the full loading of fibers before material separation.

Funding Data

- This paper was funded by the Horizon Europe grant "HORIZON-CL4-2022-RESILIENCE-01," Project MIMOSA (Project 101091826).

Conflict of Interest

There are no conflicts of interest.

Data Availability Statement

The authors attest that all data for this study are included in the paper.

References

[1] Jahn, J., Weber, M., Boehner, J., and Steinhilper, R., 2016, "Assessment Strategies for Composite-Metal Joining Technologies—A Review," Procedia CIRP, **50**, pp. 689–694.

[2] Dhilipkumar, T., and Rajesh, M., 2021, "Enhancing Strength and Stiffness of Composite Joint Through Co-Cure Technique," Compos. Commun., **27**, p. 100878.

[3] Gebhardt, J., and Fleischer, J., 2014, "Experimental Investigation and Performance Enhancement of Inserts in Composite Parts," Procedia CIRP, **23**, pp. 7–12.

[4] Guo, H., Gingerich, M. B., Headings, L. M., Hahnlen, R., and Dapino, M. J., 2019, "Joining of Carbon Fiber and Aluminum Using Ultrasonic Additive Manufacturing (UAM)," Compos. Struct., **208**, pp. 180–188.

[5] Lionetto, F., Balle, F., and Maffezzoli, A., 2017, "Hybrid Ultrasonic Spot Welding of Aluminum to Carbon Fiber Reinforced Epoxy Composites," J. Mater. Process. Technol., **247**, pp. 289–295.

[6] Bodjona, K., and Lessard, L., 2016, "Hybrid Bonded-Fastened Joints and Their Application in Composite Structures: A General Review," J. Reinf. Plast. Compos., **35**(9), pp. 764–781.

[7] Kashaev, N., Ventzke, V., Riekehr, S., Dorn, F., and Horstmann, M., 2015, "Assessment of Alternative Joining Techniques for Ti-6Al-4V/CFRP Hybrid Joints Regarding Tensile and Fatigue Strength," Mater. Des., **81**, pp. 73–81.

[8] Sarantinos, N., Tsantzalis, S., Ucsnik, S., and Kostopoulos, V., 2019, "Review of Through-the-Thickness Reinforced Composites in Joints," Compos. Struct., **229**, p. 111404.

[9] Mouritz, A. P., 2007, "Review of z-Pinned Composite Laminates," Compos. Part A Appl. Sci. Manuf., **38**(12), pp. 2383–2397.

[10] Ucsnik, S., Scheerer, M., Zaremba, S., and Pahr, D. H., 2010, "Experimental Investigation of a Novel Hybrid Metal-Composite Joining Technology," Compos. Part A Appl. Sci. Manuf., **41**(3), pp. 369–374.
[11] Stelzer, S., Ucsnik, S., and Pinter, G., 2015, "Fatigue Behaviour of Composite-Composite Joints Reinforced With Cold Metal Transfer Welded Pins," Int. J. Fatigue, **81**, pp. 37–47.
[12] Parkes, P. N., Butler, R., Meyer, J., and de Oliveira, A., 2014, "Static Strength of Metal-Composite Joints With Penetrative Reinforcement," Compos. Struct., **118**(1), pp. 250–256.
[13] Eberl, L., Avila Gray, L., Zaremba, S., and Drechsler, K., 2017, "The Effect of Fiber Undulation on the Strain Field for Pinned Composite/Titanium Joints Under Tension," Compos. Part A Appl. Sci. Manuf., **103**, pp. 148–160.
[14] Löbel, T., Kolesnikov, B., Scheffler, S., Stahl, A., and Hühne, C., 2013, "Enhanced Tensile Strength of Composite Joints by Using Staple-Like Pins: Working Principles and Experimental Validation," Compos. Struct., **106**, pp. 453–460.
[15] Graham, D. P., Rezai, A., Baker, D., Smith, P. A., and Watts, J. F., 2014, "The Development and Scalability of a High Strength, Damage Tolerant, Hybrid Joining Scheme for Composite-Metal Structures," Compos. Part A Appl. Sci. Manuf., **64**, pp. 11–24.
[16] Chang, P., Mouritz, A. P., and Cox, B. N., 2006, "Properties and Failure Mechanisms of Pinned Composite Lap Joints in Monotonic and Cyclic Tension," Compos. Sci. Technol., **66**(13), pp. 2163–2176.
[17] Arnautov, A., Nasibullins, A., Gribniak, V., Blumbergs, I., and Hauka, M., 2015, "Experimental Characterization of the Properties of Double-Lap Needled and Hybrid Joints of Carbon/Epoxy Composites," Materials, **8**(11), pp. 7578–7586.
[18] Tao, Y., Jiao, G., Wang, B., and Chang, Y., 2008, "Effect of Z-Pins' Diameter, Spacing and Overlap Length on Connecting Performance of CMC Single Lap Joint," Acta Mech. Sol. Sin., **21**(5), pp. 461–471.
[19] Tang, H., and Liu, L., 2018, "A Novel Metal-Composite Joint and Its Structural Performance," Compos. Struct., **206**, pp. 33–41.
[20] Parkes, P. N., Butler, R., and Almond, D. P., 2012, "Growth of Damage in Additively Manufactured Metal-Composite Joints," ECCM 2012—Composites at Venice, Proceedings of the 15th European Conference on Composite Materials, Venice, Italy, June 24–28, pp. 24–28.
[21] Ji, H., Kweon, J. H., and Choi, J. H., 2014, "Fatigue Characteristics of Stainless Steel Pin-Reinforced Composite Hat Joints," Compos. Struct., **108**(1), pp. 49–56.
[22] Nguyen, A. T. T., Amarasinghe, C. K., Brandt, M., Feih, S., and Orifici, A. C., 2017, "Loading, Support and Geometry Effects for Pin-Reinforced Hybrid Metal-Composite Joints," Compos. Part A Appl. Sci. Manuf., **98**, pp. 192–206.
[23] Nguyen, A. T. T., Pichitdej, N., Brandt, M., Feih, S., and Orifici, A. C., 2018, "Failure Modelling and Characterisation for Pin-Reinforced Metal-Composite Joints," Compos. Struct., **188**, pp. 185–196.
[24] Di Franco, G., Fratini, L., and Pasta, A., 2013, "Analysis of the Mechanical Performance of Hybrid (SPR/Bonded) Single-Lap Joints Between CFRP Panels and Aluminum Blanks," Int. J. Adhes. Adhes., **41**, pp. 24–32.
[25] Avgoulas, E. I., and Sutcliffe, M. P. F., 2016, "Biomimetic-Inspired CFRP to Perforated Steel Joints," Compos. Struct., **152**, pp. 929–938.
[26] Bisagni, C., Furfari, D., and Pacchione, M., 2018, "Experimental Investigation of Reinforced Bonded Joints for Composite Laminates," J. Compos. Mater., **52**(4), pp. 431–447.
[27] Bisagni, C., Furfari, D., and Pacchione, M., 2015, "Fatigue and Damage Tolerance Assessment of 3-D Reinforced CFRP Bonded Joints," 34th ICAF Conference and 28th ICAF Symposium (ICAF 2015), Helsinki, Finland, June 1–5, Vol. 1, pp. 496–509.
[28] Jürgens, M., Nogueira, A. C., Lang, H., Hombergsmeier, E., and Drechsler, K., 2014, "Influence of an Optimized 3D-Reinforcement Layout on the Structural Mechanics of Co-bonded CFRP Joints," 16th European Conference on Composite Materials (ECCM 2014), Seville, Spain, June 22–26 , pp. 22–26.
[29] Nogueira, A. C., Drechsler, K., and Hombergsmeier, E., 2012, "Analysis of the Static and Fatigue Strength of a Damage Tolerant 3D-Reinforced Joining Technology on Composite Single Lap Joints," Collection of Technical Papers —AIAA/ASME/ASCE/AHS/ASC Structures, Structural Dynamics and Materials Conference, Honolulu, HI, Apr. 23–26, pp. 1–10.
[30] Nogueira, M., Ana Carolina, D., Klaus, H., and Elke, P., 2011, "Investigation of the Properties and Failure Mechanisms of a Damage Tolerant 3D-Reinforced Joint for Lightweight Structures," SAMPE SETEC 11-International Technical Conference "Advanced Composites, The Integrated System, Leiden, The Netherlands, Sept. 14–16, pp. 537–544.
[31] Wang, X., Ahn, J., Kaboglu, C., Yu, L., and Blackman, B. R. K., 2016, "Characterisation of Composite–Titanium Alloy Hybrid Joints Using Digital Image Correlation," Compos. Struct., **140**, pp. 702–711.
[32] Jansson, A., and Pejryd, L., 2019, "Dual-Energy Computed Tomography Investigation of Additive Manufacturing Aluminium–Carbon-Fibre Composite Joints," Heliyon, **5**(2), p. e01200.
[33] Tu, W., Wen, P. H., Hogg, P. J., and Guild, F. J., 2011, "Optimisation of the Protrusion Geometry in ComeldTM Joints," Compos. Sci. Technol., **71**(6), pp. 868–876.
[34] Raimondi, L., Tomesani, L., Donati, L., and Zucchelli, A., 2021, "Lattice Material Infiltration for Hybrid Metal–Composite Joints: Manufacturing and Static Strength," Compos. Struct., **269**, p. 114069.
[35] Graziosi, S., Cannazza, F., Vedani, M., Ratti, A., Tamburrino, F., and Bordegoni, M., 2020, "Design and Testing of an Innovative 3D-Printed Metal–Composite Junction," Addit. Manuf., **36**, p. 101311.
[36] Coluccia, A., Jiang, G., Meyer, G., De Pasquale, G., and Mittelstedt, C., 2022, "Nonlinear Static and Dynamic Modeling of Energy Absorption Lattice Structures Behavior," Mech. Adv. Mater. Struct., **30**(14), pp. 1–12.
[37] De Pasquale, G., Luceri, F., and Riccio, M., 2019, "Experimental Characterization of SLM and EBM Cubic Lattice Structures for Lightweight Applications," Exp. Mech., **59**(4), pp. 469–482.
[38] De Pasquale, G., Luceri, F., and Riccio, M., 2019, "Experimental Evaluation of Selective Laser Melting Process for Optimized Lattice Structures," Proc. Inst. Mech. Eng. Part E J. Process Mech. Eng., **233**(4), pp. 763–775.
[39] De Pasquale, G., and Mura, A., 2018, "Dynamic Response Evolution of Damaged SLM Lattice Structures," Proceedings of the 1st International Conference on Mechanics of Advanced Materials and Structures (ICMAMS), Torino, Italy, June 17–20.
[40] De Pasquale, G., Luceri, F., and Romeo, M., 2018, "SLM-EBM Processes Optimization for Metal Lattice Structures Fabrication," Proceedings of the 1st International Conference on Mechanics of Advanced Materials and Structures (ICMAMS), Turin, Italy, June 17–20.
[41] De Pasquale, G., and Tagliaferri, A., 2021, "Modeling and Characterization of Mechanical and Energetic Elastoplastic Behavior of Lattice Structures for Aircrafts Anti-icing Systems," Proc. Inst. Mech. Eng. Part C J. Mech. Eng. Sci., **235**(10), pp. 1828–1839.
[42] De Pasquale, G., and Sibona, S., 2021, "Hybrid Materials Based on Polymers-Filled AM Steel Lattices With Energy Absorption Capabilities," Mech. Adv. Mater. Struct., **29**(18), pp. 1–13.
[43] Coluccia, A., De Pasquale, G., Meyer, G., and Mittelstedt, C., 2021, "Modeling of Lattice Structures Energy Absorption Under Impact Loads," 2021 12th International Conference on Mechanical and Aerospace Engineering (ICMAE 2021), Virtual, July 16–19, pp. 494–499.
[44] De Pasquale, G., Plos, S., and Zappulla, L., 2022, "Modeling and Validation of AM Metals/CFRP Joints Based on Patterned Surfaces and Fibers Engagement," Key Eng. Mater., **913**, pp. 293–299.
[45] De Pasquale, G., 2020, "Struttura alare basata su elementi metallici conformati e relativo metodo di realizzazione," Patent No. IT102020000012619.
[46] De Pasquale, G., 2023, "Giunzione comprendente protuberanze con geometria ottimizzata," Patent No. IT102023000006393.
[47] BSI, 2021, "BS ISO 22841:2021 Composite and Reinforcement Fibres. Carbon Fibre Reinforced Plastics (CRFPs) and Metal Assemblies. Determination of the Tensile Lap-Shear Strength," BSI, https://bsol-bsigroup-com.oxfordbrookes.idm.oclc.org/PdfViewer/Viewer?pid=000000000030377313
[48] Bertolino, G., Montemurro, M., and De Pasquale, G., 2019, "Multi-scale Shape Optimisation of Lattice Structures: An Evolutionary-Based Approach," Int. J. Interact. Des. Manuf., **13**(4), pp. 1565–1578.
[49] De Pasquale, G., and Coluccia, A., 2022, "Fatigue Failure Prediction in Lattice Structures Through Numerical Method Based on De-homogenization Process," Procedia Struct. Integr., **41**, pp. 535–543.